Nuclear Inst. and Methods in Physics Research, A 1031 (2022) 166568

Contents lists available at ScienceDirect

Nuclear Inst. and Methods in Physics Research, A

journal homepage: www.elsevier.com/locate/nima

Photon detector response function methodology using MCNP and shift hybrid radiation transport code for wide-area contamination assay applications

E. Asano [a], D. Coleman [b], G. Davidson [c], S. Dewji [a,*]

[a] Nuclear and Radiological Engineering and Medical Physics Programs, George W. Woodruff School of Mechanical Engineering, Georgia Institute of Technology, Atlanta, GA 30313, USA
[b] Department of Medical Physics, University of Wisconsin-Madison, Madison, WI 53705, USA
[c] Oak Ridge National Laboratory, Oak Ridge, TN 37830, USA

ARTICLE INFO

Keywords:
Gamma-ray spectroscopy
Radiation transport
Monte Carlo
Deterministic solver
Environmental assay
Decommissioning

ABSTRACT

Radiation transport modeling using the Monte Carlo N-Particle (MCNP) radiation transport code and Monte Carlo code, Shift, were employed to model detector responses for a variety of wide-area photon contamination scenarios. In this study, $2'' \times 2''$ and $3'' \times 3''$ cylindrical NaI(Tl) scintillation detector configurations at source detector-distances of 0.5 cm, 1 cm, 2.54 cm, 10 cm, and 30 cm were modeled. Media of soil, concrete, and steel were evaluated for contamination depths ranging from surface to a depth of an infinite thickness in each medium for photon energies ranging from 20 keV to 3 MeV, which correspond to the energies that current detectors can discern. Monoenergetic photon surface contamination detector responses for each of the media, source–detector distances, and detectors were estimated using MCNP v6.2. Shift was harnessed for improved variance reduction of particle transport in highly attenuating media to obtain average cell fluxes in the two MCNP NaI(Tl) scintillation detector configurations. Average cell flux values in Shift were coupled with detector responses from MCNP to convert average cell flux in a void to energy distribution of pulses in the NaI(Tl) scintillation detector crystal of interest. An optimized detector response function methodology was developed by coupling the MCNP radiation transport method with the Consistent Adjoint Driven Importance Sampling (CADIS) hybrid radiation transport method built into Shift to significantly decrease the runtime of thousands of MCNP pulse height simulations. The methodology may be utilized to quickly and accurately facilitate the assessment of a broad range of wide-area environmental contamination assay and decommissioning cleanup applications.

1. Introduction

A wide variety of sites around the world exist for the production, handling, and/or storage of radioactive materials. Such sites may require the use of standardized remediation (i.e., cleanup) and surveying procedures prior to site release for restricted use or unrestricted public use [1–5]. According to the Multi-Agency Radiation Survey and Site Investigation Manual (MARSSIM), surveying procedures consist of four main phases for a contaminated site: *plan* (characterize the level of contamination and decide upon appropriate measurement technique(s)), *implement* (data acquisition), *assess* (data verification and validation), and *decide* (decide if a survey unit demonstrates regulatory compliance) [1]. In the United States, the decommissioning process following remediation at a contaminated site must demonstrate regulatory compliance by conducting surveys to ensure that a specific regulatory limit has been met prior to site release [1]. As an example, the regulatory limit may be defined as an annual dose rate or risk to a receptor in an environmental setting [1–5]. In order to ensure that compliance is met for such a wide variety of potentially contaminated sites, a scientifically rigorous and regulation-compliant approach should be followed by stakeholders prior to making a site release decision. One such approach for establishing site release criterion has been provided by the MARSSIM [1], which consists of three major steps: *translate*, *measure*, and *decide*. The *measure* step may consist of an extremely large amount of survey and sample measurements in a real-world potentially contaminated radiological site [1]. Thus, the use of radiation transport simulation methods may facilitate wide-area environmental contamination assay planning and decommissioning cleanup applications by enhancing the utility of modeling and simulation tools while reducing the resource burden associated with current surveying and sampling procedures.

In this study, capabilities of the Monte Carlo N-Particle Version 6.2 (MCNP v6.2) [6] and Shift [7,8] radiation transport codes were harnessed to estimate detector responses (i.e., scintillation detector pulse

* Corresponding author.
E-mail address: shaheen.dewji@gatech.edu (S. Dewji).

https://doi.org/10.1016/j.nima.2022.166568
Received 7 January 2022; Received in revised form 28 February 2022; Accepted 6 March 2022
Available online 18 March 2022
0168-9002/

heights) for computationally intensive wide-area contamination radiation detection problems. MCNP is a general-purpose, stochastic radiation transport code that statistically samples individual particle behavior to estimate an average result. Shift is a new state-of-the-art Monte Carlo (MC) code developed at Oak Ridge National Laboratory (ORNL) that implements hybrid radiation transport techniques [9]; predecessor hybrid radiation transport codes at ORNL include MAVRIC [10] and the AutomateD VAriaNce reducTion Generator (ADVANTG) [11]. The particle random history sampling process is very time consuming over such wide-area contamination problem geometries in MCNP. The problems are deemed to be difficult, especially when buried source (volumetric source) attenuation is simulated. In addition, the problems are difficult since they consist of extremely large unimportant regions accompanied by relatively small tally volumes (i.e., few particles contribute to the tally), and thus require many particle histories to obtain statistically reliable results.

MCNP has the limitation of being computationally expensive when using implicit capture without any additional variance reduction (VR) techniques (default MCNP), where particles are never lost due to absorption [12,13]. Ref. [12] further describes implicit capture, and Ref. [13] additionally elaborates on how it may be computationally expensive. However, the pulse height tally is an exception to all other tallies in MCNP, since it implements analog capture (which can be extremely time-consuming) by default unless the forced collision VR technique in MCNP is used [6,14]. MCNP offers a wide variety of VR techniques for pulse height tallies, including the DXTRAN (deterministic transport) sphere technique, which is particularly useful for improving particle sampling in small tally regions that are difficult to sample (prevalent in wide-area contamination transport problems) [6,14]. As the energy of the source decreases, the efficiency of the DXTRAN VR technique diminishes for such wide-area contamination problems, where it can take hours to estimate a statistically reliable result when simulating in parallel. In contrast to many VR techniques in MCNP, the use of modern automated VR capabilities (i.e., hybrid VR) requires little experience, time, and effort of the user to effectively implement [9]. Thus, the built-in hybrid VR capabilities in Shift were exploited to make a variety of buried source, wide-area photon contamination pulse height tally simulations in MCNP feasible.

1.1. The Monte Carlo (MC) method

The Monte Carlo (MC) method is a stochastic method that is widely used to solve radiation transport problems in reactor physics, shielding, dosimetry, radiation detection and measurements, and various other applications of interest. The method is stochastic in that it relies upon statistical sampling from relevant probability density functions in a phase space to describe average particle behavior in a given simulation environment. The behavior of a simulated particle is determined by the types of sampled interactions or events (capture, scatter, leakage, etc) as the simulated particle is tracked through the problem domain. The lifetime of an individual particle from birth until termination (due to absorption or escape from the problem boundary) is described as its random "history". An example of two particle random histories is visually depicted by Fig. 1 [14].

While the MC method is considered the most accurate method for computing solutions to the radiation transport equation, it can be computationally expensive, depending on the complexity of the problem. Quantities of interest (such as dose) are calculated using *tallies*. The dose in a region of interest is accumulated every time a particle history passes through that region. For many realistic problems of interest, these tallies can be slow to converge, requiring many particle histories to reduce the statistical variance of the tally to acceptable levels. MC codes mitigate this expense using a variety of VR techniques.

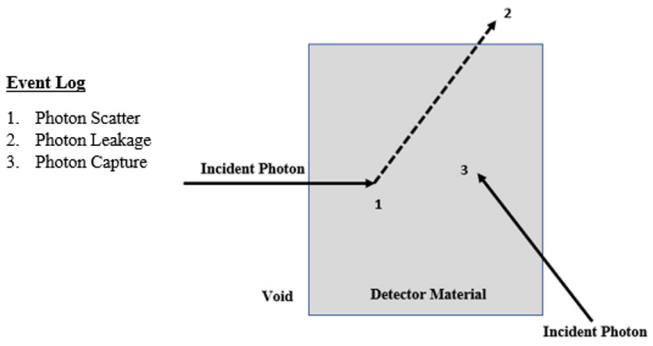

Fig. 1. The random history of two photons in an arbitrary detector material [14].

1.2. Monte Carlo N-particle (MCNP) radiation transport code

One of the most popular MC radiation transport codes is MCNP, developed at Los Alamos National Laboratory [14]. MCNP features continuous-energy physics for multiple particle types, as well as a wide array of statistical tallies, which can be used to compute various values of interest. MCNP features a variety of VR techniques, including one of the most powerful VR techniques: weight windows [15]. It is difficult for the user to manually estimate high quality weight windows without sufficient knowledge of the problem response [16]. In other words, it is difficult for the user to guess the expected contribution to the tally in the space-energy domain throughout the entire phase space, especially with large problems. Hence, a method for automatically computing optimal weight windows and consistently biased sources (statistical weights of source particles are within weight window bounds to avoid unnecessary splitting/rouletting upon birth) is desirable for increasing the efficiency of the wide-area contamination problems [9]. However, MCNP does not automatically compute optimal weight windows or consistently biased sources for the type of wide-area contamination problems often used in site remediation. MCNP offers a weight window generator for automatically computing weight windows; however, it is an iterative process for computing optimal weight windows and thus requires extensive time to effectively utilize [11].

1.3. Shift: A massively parallel Monte Carlo radiation transport code

Shift is a massively parallel, (scaling from laptops to supercomputers) neutral particle MC package within the Exnihilo suite of radiation transport tools developed by Oak Ridge National Laboratory (ORNL) [7,8]. Shift has an automated hookup to a deterministic transport solver that can be used to automatically generate weight windows and consistently biased sources to accelerate the statistical convergence rate of stochastic MC radiation particle transport solutions. This enables Shift to efficiently produce low-variance solutions to the radiation transport equation in difficult, deep penetration problems. However, Shift lacks pulse height tallies, and requires a user-specified detector response function that converts a particle flux in a tally cell to a pulse height spectrum.

2. Methodology

Shift does not currently offer a pulse height tally; hence, a detector response function methodology was developed to estimate the pulse height tallies in Shift. The aforementioned methodology may be applied and expanded to facilitate evaluation of site release criterion approaches as provided by MARSSIM or similar international guideline approaches that may exist.

2.1. Detector response function implementation

The goal of this study is to propose a detector response methodology that may be used to increase the efficiency of thousands of pulse height tally estimations for facilitating complex and computationally expensive wide-area environmental assay and decommissioning cleanup applications. These wide-area site remediation problems that require the simulation of buried source attenuation can be computationally expensive. To make these calculations tractable, we developed a method to combine the efficiency of Shift's VR capabilities with the improved tally capabilities of MCNP through actuation of the following key steps:

1. Simulating a prescribed MCNP surface contamination scenario to estimate the energy-binned[1] pulse height in a prescribed full detector model NaI crystal at a prescribed monoenergetic source energy;
2. Simulating the equivalent monoenergetic source surface contamination scenario described by (1) using hybrid MC in Shift, but filling the entire detector with a void material (i.e., coupling surface) and estimating the energy-binned average cell flux in the void detector;
3. Computing the detector response function for the contamination scenario described by (1) and (2) by dividing the tally result of (1) by the tally result of (2);
4. Simulating the scenario described by (2) using hybrid MC in Shift, but with a prescribed buried source rather than a surface source; and
5. Normalizing the energy-binned tally result of (4) by the appropriate detector response function group[2] computed by (3) through piecewise cubic hermite interpolating polynomial (PCHIP) interpolation in a post-processing script to estimate the Shift detector response. The PCHIP algorithm may be briefly explained by Eq. (1); further details may be found in the literature [17,18].

In the PCHIP algorithm, when interpolating for a given variable y_k at point x_k, the first derivatives at the points x_k, f'_k may be utilized. Let $h_k = x_{k+1} - x_k$, and $d_k = \left(y_{k+1} - y_k\right)/h_k$ (slopes at internal points x_k). If $f'_k \neq 0$, then the weighted harmonic mean is as follows [19]:

$$\frac{w_1 + w_2}{f'_k} = \frac{w_1}{d_{k-1}} + \frac{w_2}{d_k}, \tag{1}$$

where w_1 is equal to $2h_k + h_{k-1}$ and w_2 is equal to $h_k + 2h_{k-1}$.

A sample VisEd representation of the response function implementation in MCNP for a $2'' \times 2''$ NaI(Tl) detector problem is shown in Fig. 2 [20]. The MCNP full detector model and Shift detector void model relationship is given by Eq. (2). Hence, in the Shift volumetric contamination models, the average cell flux in a void detector was converted to a full detector model pulse height after normalizing by the appropriate detector response function group, as shown by Eq. (3).

The MCNP/Shift detector response function is given by

$$RF_i\left(pulse - cm^2\right) = \frac{\left(\frac{pulse}{sp}\right)_{Full,i}}{\left(\frac{1}{cm^2 - sp}\right)_{Void,i}}, \tag{2}$$

where RF_i is the response function for a specific contaminated medium, detector configuration, source–detector distance, and monoenergetic source energy, i; $\left(\frac{pulse}{sp}\right)_{Full,i}$ is the MCNP full model surface contamination pulse (detector count) per source particle (sp) at monoenergetic source energy, i; and $\left(\frac{1}{cm^2 - sp}\right)_{Void,i}$ is the corresponding Shift surface contamination average cell flux in a void detector at monoenergetic source energy, i.

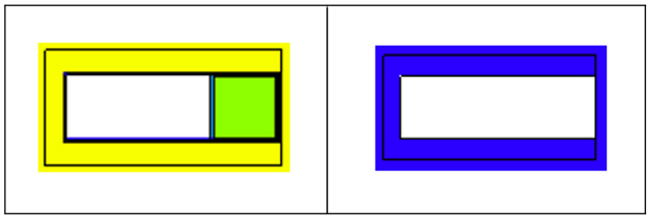

Fig. 2. A full model $2'' \times 2''$ NaI(Tl) detector (left) and corresponding void detector (right). Each detector model is housed in a universe filled with air. The full model surface contamination response (MCNP pulse height) in the detector crystal (left, green region) is divided by the corresponding Shift surface contamination average cell flux in the void detector region (right, white region) to generate a detector response function [20].

The final detector response relationship is

$$Response = \sum_{i=1}^{1024} \begin{pmatrix} Average\ Cell\ Flux \\ in\ a\ Void\ Detector \end{pmatrix}_i (RF)_i, \tag{3}$$

where *Response* is the Shift volumetric contamination final detector response $(pulse/sp)$; $\begin{pmatrix} Average\ Cell\ Flux \\ in\ a\ Void\ Detector \end{pmatrix}_i$ is the Shift volumetric contamination average cell flux in a void detector for a specific contamination medium and depth, detector configuration, source–detector distance, and energy bin, i; and $(RF)_i$ is the interpolated response function at energy bin, i.

2.2. Consistent adjoint driven importance sampling (CADIS) method

The Shift surface and volumetric contamination average cell fluxes in Eqs. (2) and (3), respectively, were estimated with the use of a hybrid radiation transport method. The hybrid radiation transport method utilized in this study is known as the Consistent Adjoint Driven Importance Sampling (CADIS) method [9], which is a single tally region optimization method. The implementation of CADIS in Shift relies on the 3D multi-group discrete ordinates adjoint transport solver, Denovo, to compute the adjoint flux [21]. An importance map may be generated by taking the inverse of the adjoint flux [9]. The importance map is a measure of the importance of a region of phase space to the requested tally, where particles in important regions of phase space are more likely to contribute meaningfully to the tally results.

From this importance map, weight windows may be constructed. When a particle history enters a region of phase space, its statistical weight is compared to the lower and upper bounds of the weight window. Particles with statistical weights below the weight window are rouletted, while particles with weights above the weight windows are split. This ensures that the bulk of the computational effort is directed to important particle histories (i.e., particle histories that are likely to contribute meaningfully to the requested tally). The lower bound of a weight window in a given phase-space region, $w_l\left(\vec{r}, E\right)$, is defined by Eq. (4) [9]:

$$w_l\left(\vec{r}, E\right) = \frac{R}{\phi^+\left(\vec{r}, E\right)\left(\frac{c+1}{2}\right)}, \tag{4}$$

where $w_l\left(\vec{r}, E\right)$ is the lower bound statistical weight, c is the ratio of the upper and lower weight window bounds $\left(c = w_u/w_l\right)$, R is the total detector response, and $\phi^+\left(\vec{r}, E\right)$ is the scalar adjoint flux.

Additionally, the adjoint flux can be used to bias the source such that particles are more likely to be born in regions of higher importance. The biased source is constructed using Eq. (5) [9]:

$$\hat{q}\left(\vec{r}, E\right) = \frac{\phi^+\left(\vec{r}, E\right) q\left(\vec{r}, E\right)}{R}, \tag{5}$$

[1] All tallies in this study were binned into 1024 energies to emulate a multi-channel analyzer (MCA).

[2] In total, there were 30 detector response function groups (each containing 19 monoenergetic photon sources at varying contamination depths), comprising three contaminated media, two NaI(Tl) detector configurations, and five source–detector distances.

where $\hat{q}(\vec{r}, E)$ is the biased source and $q(\vec{r}, E)$ is the unbiased source. The deterministic Denovo solver generates the adjoint importance function and associated importance map; the Shift MC solver then employs a stochastic splitting/roulette method in the phase space while simulating particle histories in order to maximize contributions to the tally region. This hybrid technique greatly increases the rate at which the Shift MC tallies statistically converge compared to MC simulations that only use the implicit capture VR technique. It should be noted that the Forward-Weighted Consisted Adjoint Driven Importance Sampling (FW-CADIS) hybrid radiation transport method [22] may have been utilized to further reduce the computational effort required of this study. However, utilizing the FW-CADIS method for estimating the prescribed monoenergetic detector response functions would require further analysis for implementation in an advanced implementation of radiation transport codes.

It should be noted that multiple implementations of hybrid radiation transport capabilities exist for increasing the efficiency of wide-area photon contamination problems, including Shift [7,8], MAVRIC [10], and the AutomateD VAriaNce reducTion Generator (ADVANTG) [11]. However, Shift is advantageous since it is fully integrated (i.e., VR parameters are fed into the MC solver directly in a single simulation) and has very good parallel scalability. Shift is also geometry agnostic in contrast to MAVRIC and ADVANTG.

2.3. Weight window precalculation method

When the CADIS hybrid method in Shift is employed, a massive Hierarchical Data Format (HDF) file (order of gigabytes) that stores the importance map of the problem is generated. Each time that a CADIS hybrid method problem is simulated, a varying amount of computational runtime is required to generate the importance map. Shift employs a method for implementing precalculated importance maps in the CADIS hybrid simulations in order to eliminate redundancies associated with the generation of importance maps. The weight window precalculation method may be implemented if the geometry, materials, and location of a single tally region in the problem is constant; therefore, the single tally optimization CADIS hybrid method in this study may be compatible with the weight window precalculation method.

The weight windows are a function of space and energy across the problem geometry as shown by Eq. (4) [9]. The weight windows will be constant for any source energy spectrum and contamination depth, so long as the contaminated medium type, detector configuration, and source–detector distance are constant. This is the case since the importance maps are optimized for a localized tally based on the multi-group cross section library energy bounds defined in the problem, and not the source energy spectrum and contamination depth defined for Shift MC transport. The weight window precalculation method was employed by simulating a CADIS hybrid method problem with one source particle at any energy and contamination depth for the contaminated medium type, detector configuration, and source–detector distance of interest. The HDF file containing the importance map may be automatically loaded into the Shift volumetric contamination problems for a given response function group. This resulted in 30 HDF files being generated (akin to 30 response function groups or importance maps), as opposed to thousands (one for each simulation).

3. Model description and preliminary benchmarks

3.1. Model description and materials data

The ability to conduct rapid, high-fidelity radiation transport simulations was paramount given the need for 3800 discrete simulations for a series of 19 monoenergetic photon energies, contamination depths, source–detector distances, and NaI(Tl) detector models as summarized in Table 1 below.

In this study, all radiation transport problems in Shift were modeled as MCNP5 v1.6 geometries using the fixed-source solver in photon mode. Primary gamma-ray emissions alone were considered due to Shift's lack of charged particle transport. Hence, simulating the detector response contribution from bremsstrahlung radiation produced from primary or secondary electron attenuation in the media is currently omitted, but under current investigation in an upcoming study. The bremsstrahlung contribution to the detector response (and thus dose to the receptor) becomes significant for radionuclides that only emit beta particles (i.e., ^{85}Kr, ^{90}Sr) [23,24]. The lack of charged particle transport in Shift will have little effect on the detector responses in this study for the photon mode problems, where the majority of the response is due to primary source photons interacting in the detector crystal.

Parameters modeled included the following: contaminated media radii, discrete monoenergetic photon energies, NaI(Tl) scintillation detector configurations, source–detector distances, and source material compositions. Source–detector distances of 0.5 cm, 1 cm, 2.54 cm, 10 cm, and 30 cm were modeled. Media of soil, concrete and steel were evaluated for the following contamination depths: ground plane, 1 cm, 2 cm, 3 cm, 5 cm, 15 cm, and infinite depth. The following 19 discrete monoenergetic photon energies were evaluated: 0.02 MeV, 0.03 MeV, 0.04 MeV, 0.05 MeV, 0.06 MeV, 0.07 MeV, 0.08 MeV, 0.1 MeV, 0.15 MeV, 0.2 MeV, 0.3 MeV, 0.4 MeV, 0.5 MeV, 0.6 MeV, 0.8 MeV, 1 MeV, 1.5 MeV, 2 MeV, and 3 MeV.

The prescribed models consisted of a cylindrical environment with a cylindrical NaI(Tl) detector surrounded by air placed at varying distances from a contaminated source medium. The model parameters varied as a function of the prescribed NaI(Tl) detector configuration, source–detector distance, medium type, and contamination depth. The energy of the primary gamma-ray source was selected as the basis upon which to simulate infinite depth contamination and the wide-area contamination plane radius. For a given gamma-ray energy, four mean free paths in the medium of interest determined the infinite contamination depth, whereas four mean free paths in air determined the radius of the wide-area contamination plane [25]. Four mean free paths represent a transmission of 1.8% of photons in good geometry; this implies that the photons will be sufficiently attenuated prior to detection. The number of prescribed simulations in Table 1 were revised due to some depth thicknesses exceeding four mean free paths in certain media. It was, therefore, identified as unnecessary to conduct volumetric depth simulations in which the prescribed volumetric depth exceeded the infinite thickness. A sample computer-aided design (CAD) rendering of the contamination problem modeled in MCNP and Shift is depicted in Fig. 3 [26]. Materials data for modeling in MCNP/Shift was obtained from Ref. [27], with the exception of the silty soil composition, which was obtained from Ref. [24].

The medium (and world boundary) in Fig. 3 radius is defined by 4 mean free paths in air at 3 MeV (highest source energy) to enable sufficient source attenuation prior to detection. The source (inner red cylindrical region) radius is defined by 4 mean free paths as a function of medium type and monoenergetic source energy. The distance from the medium surface to the edge of the world boundary behind the detector is always defined by 4 mean free paths in air at 3 MeV to account for skyshine.

3.2. Preliminary benchmarks

Benchmark simulations were conducted to compare the computational runtimes between MCNP and hybrid Shift under the same modeling conditions as an initial step in this study. A short description of each modeling case is given in Table 2.

In addition to the computational runtime benchmarks, preliminary average cell flux tally benchmark comparisons between MCNP and hybrid Shift were conducted. Since average cell flux obtained in Shift would eventually be converted to an MCNP-equivalent pulse height, it was imperative to demonstrate convergence between the two transport

Table 1
Breakdown of simulation runs for obtaining the detector response data.

Medium	Monoenergetic energies	Contamination depths	Source–detector distances	Number of detectors	Total runs
Concrete	19	7	5	2	1,330
Soil	19	7	5	2	1,330
Steel (304L)	19	6	5	2	1,140
TOTAL					3,800

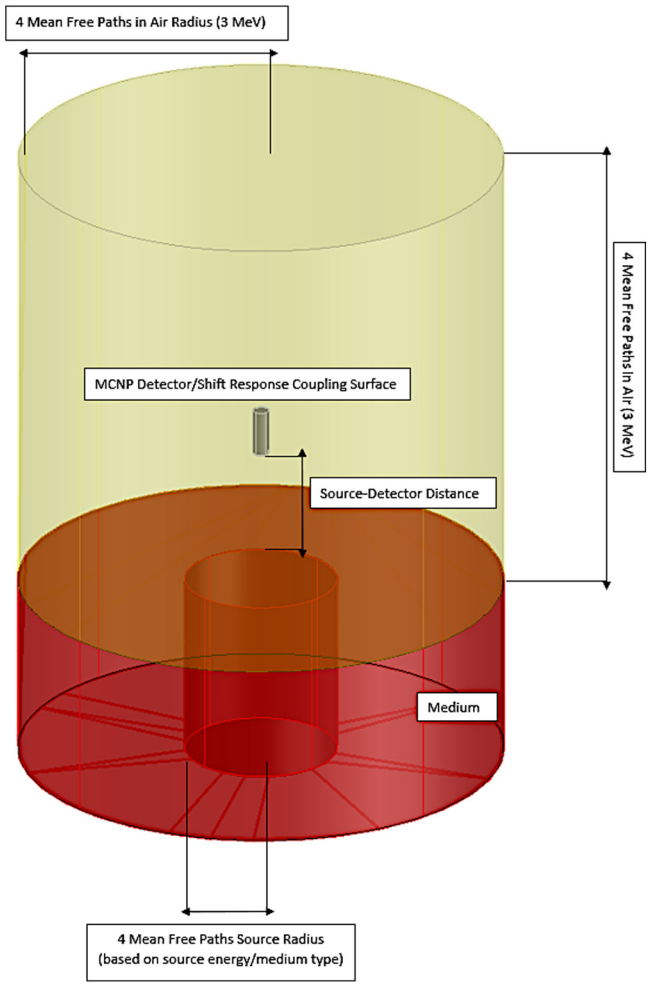

Fig. 3. Example CAD model of the wide-area contamination problem geometry with a buried source (*not to scale*). The full detector model in MCNP/Shift response coupling surface (gray cylinder) is surrounded by a cylinder filled with air (yellow region). The prescribed medium (including outer and inner red cylindrical regions) and monoenergetic, uniformly buried source (inner red cylindrical region) is depicted.

Table 2
Initial benchmark modeling case descriptions.

Case	Modeling description
1	A cylindrical environment consisting of monoenergetic photon contamination in soil surrounded by air. A cylindrical isotropic surface contamination case (1 cm source thickness), as well as a cylindrical isotropic volumetric contamination case were modeled (100 cm source thickness) in the z-direction. Average cell flux was tallied over an air cylinder at 30 cm away from the source for both scenarios. A rectangular parallelepiped world boundary extending 32 cm in the +z-direction was modeled.
2	Equivalent to Case 1. However, the rectangular parallelepiped world boundary extended 100,000 cm in the +z-direction to observe the effects of skyshine.

Table 3
Initial computational runtime benchmark of the CADIS hybrid method in Shift compared to MCNP v6.2. The total computational runtime in this benchmark includes all events that take place from job execution until termination. All simulations were run on the ORNL Romulus (2.8 GHz AMD Opteron 6320) machine with 8 nodes and 32 CPU cores per node.

Case	Total MCNP runtime (minutes)	Total shift runtime (minutes)	Percent difference
1	61.58	3.33	94.59%
2	59.63	4.88	91.82%

methods. The average cell fluxes were tallied over a void box for 50 keV, 100 keV, 500 keV, 1 MeV, and 3 MeV monoenergetic sources buried in 1 cm of contaminated soil in Shift and MCNP. The source–detector distance for all runs was 10 cm; however, limiting source radii and world boundary dimensions were chosen for the purpose of demonstrating the convergence of Shift and MCNP transport methods for tallying average cell flux. The default lower energy cutoff in Shift is 10 keV; therefore, a 10 keV energy cutoff was employed in MCNP. It should be noted that in the production simulations, the Shift lower energy cutoff was specified at 1 eV (equivalent to MCNP default). The results of the computational runtime and average cell flux comparison benchmarks are summarized next. All benchmark and production runs were simulated in MCNP and Shift using parallel computing resources with 8 nodes and 32 CPU cores per node. In addition, the tally convergence criteria for all benchmark and production run were less than a 5% relative error (inclusive of average cell flux and pulse height).

4. Results and discussion

4.1. Computational runtime benchmark

A benchmark of CADIS hybrid method capabilities demonstrated that radiation transport of photons through contaminated volumetric depths significantly superseded capabilities of MCNP v6.2 for simulations of track length estimate of average cell flux. Table 3 below summarizes the initial benchmark comparison for the two modeling cases described in Table 2.

4.2. Average cell flux convergence benchmark

The results of the average cell flux convergence benchmark described in Section 3.2. are summarized in Table 4. The preliminary results demonstrate that under the same modeling conditions the detector response output in Shift is expected to converge well with MCNP when converting average cell flux to pulse height at each interpolated energy bin. A comparison of the MCNP and Shift average cell flux distribution over each energy spectrum corresponding to Table 4 is shown in Figs. 4, 6, 8, 10 and 12. The ratio of MCNP and Shift average cell flux over each energy spectrum is given by Figs. 5, 7, 9, 11 and 13. It is worth noting that the average cell flux in MCNP and Shift decreases significantly in magnitude as the energy decreases from the photopeak energy bin for each source spectrum (the average cell flux decreases by up to six orders of magnitude from the photopeak energy bin in some cases), which results in seemingly skewed MCNP and Shift average cell flux ratios at select energies. The differences in the results between Shift and MCNP become more pronounced as the energy decreases for each

Table 4
Results of the preliminary average cell flux convergence tests.

Energy (MeV)	MCNP average cell flux	Shift average cell flux	Percent error (1σ)
0.05	$8.237 \times 10^{-5} \pm 0.10\%$	$8.240 \times 10^{-5} \pm 0.12\%$	0.035%
0.1	$1.213 \times 10^{-4} \pm 0.08\%$	$1.212 \times 10^{-4} \pm 0.09\%$	0.036%
0.5	$1.343 \times 10^{-4} \pm 0.07\%$	$1.346 \times 10^{-4} \pm 0.08\%$	0.169%
1	$1.282 \times 10^{-4} \pm 0.08\%$	$1.279 \times 10^{-4} \pm 0.08\%$	0.230%
3	$1.194 \times 10^{-4} \pm 0.08\%$	$1.176 \times 10^{-4} \pm 0.08\%$	1.505%

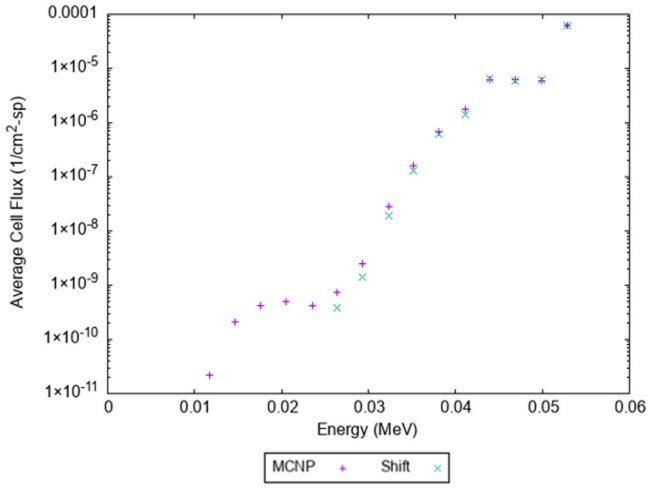

Fig. 4. Average cell flux comparison over the 50 keV source spectrum. A maximum value is observed at the 50 keV energy bin, which corresponds to a photopeak when converted to a pulse height.

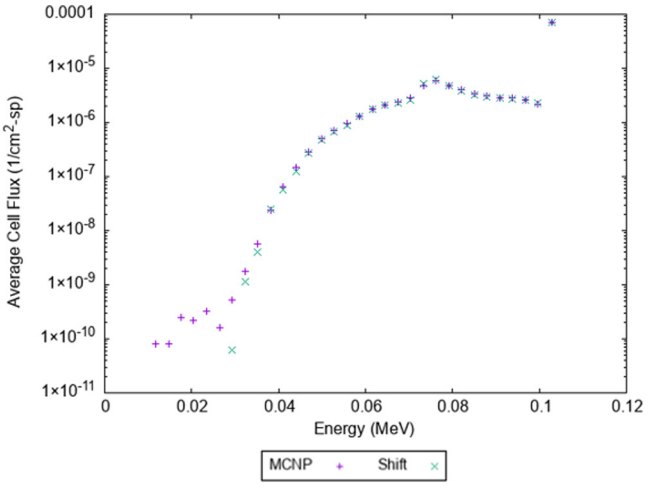

Fig. 6. Average cell flux comparison over the 100 keV source spectrum. A maximum value is observed at the 100 keV energy bin, which corresponds to a photopeak when converted to a pulse height.

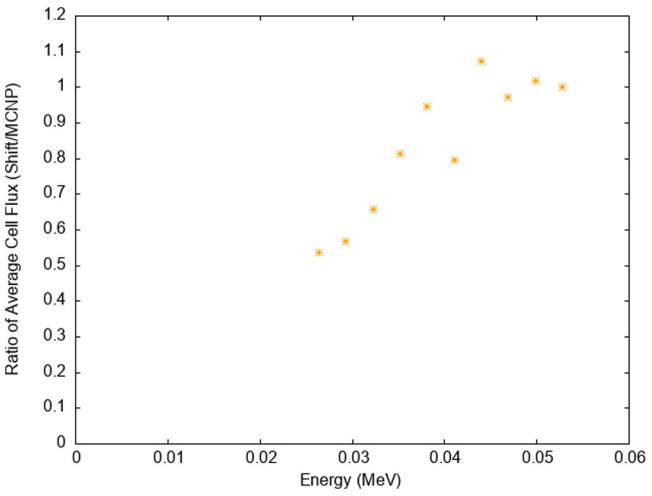

Fig. 5. Ratio of Shift and MCNP average cell flux over the 50 keV source spectrum.

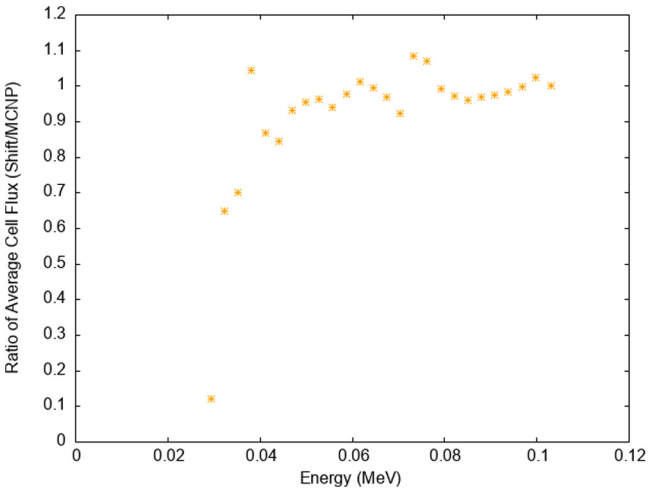

Fig. 7. Ratio of Shift and MCNP average cell flux over the 100 keV source spectrum.

source spectrum. This is due to Shift's lack of data and treatment for bremsstrahlung reactions, which resulted in a lack of data points for Shift at very low energies [7,28]. Based on the results, the use of the MCNP/Shift detector response methodology is predominantly limited to photon energies above 0.04 MeV when analyzing a primary photon source energy spectrum. However, the discrepancies shown at energies below 0.04 MeV of each spectrum have little effect on the total detector response when converting average cell flux to pulse height.

4.3. Adjoint flux distribution

The sample adjoint flux distribution comparison is shown for a 2″ × 2″ NaI(Tl) detector simulation at a source–detector distance of 2.54 cm for soil contamination. The adjoint flux distribution is represented by two different energy groups defined in the SCALE "v7.1-28n19g" multi-group (MG) library [28]. The MG library contains 19 energy groups in descending order ranging from 20 MeV down to 10 keV. In Figs. 14 and 15, the adjoint flux distribution is not superimposed over the constructed solid geometry (CSG) model; however, it should be noted that the detector would be centered at 2.54 cm from x=0 along the negative x-axis (adjacent to the tally region). The cylindrical soil radius spans over four mean free paths in air at 3 MeV ($\pm$86388.74 cm along the y-axis) for any given soil simulation; the contaminated soil radius will vary as a function of source energy. In Fig. 14 and 15, the soil depth spans from x=0 to x=+67.69 cm (infinite depth). Hence, superimposing the adjoint flux distribution over the CSG model would be of little value for the purposes of this demonstration, since the detector and soil

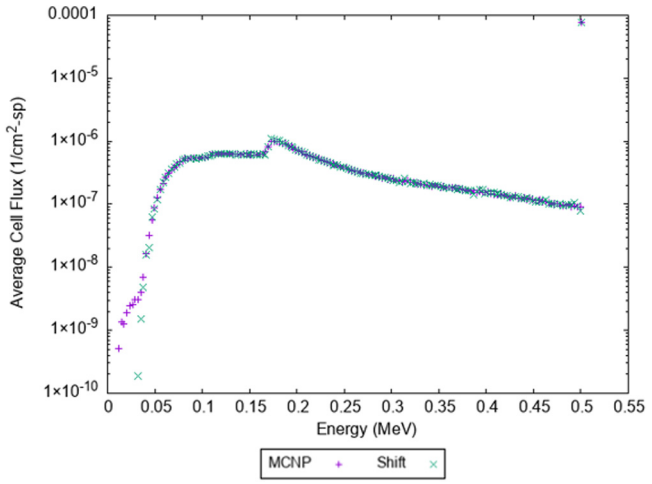

Fig. 8. Average cell flux comparison over the 500 keV source spectrum. A maximum value is observed at the 500 keV energy bin, which corresponds to a photopeak when converted to a pulse height.

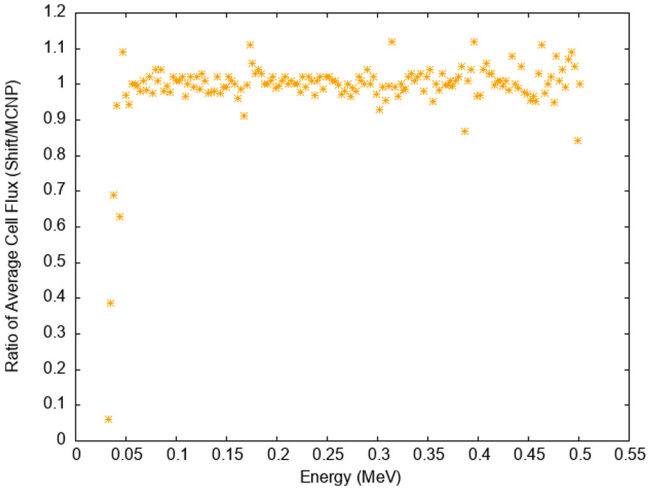

Fig. 9. Ratio of Shift and MCNP average cell flux over the 500 keV source spectrum.

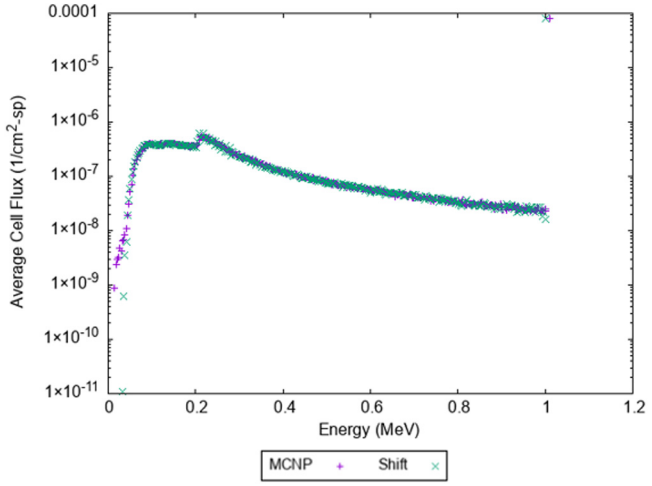

Fig. 10. Average cell flux comparison over the 1 MeV source spectrum. A maximum value is observed at the 1 MeV energy bin, which corresponds to a photopeak when converted to a pulse height.

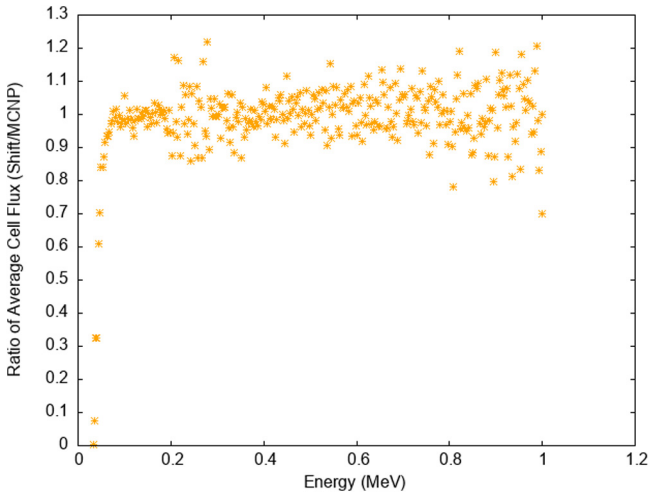

Fig. 11. Ratio of Shift and MCNP average cell flux over the 1 MeV source spectrum.

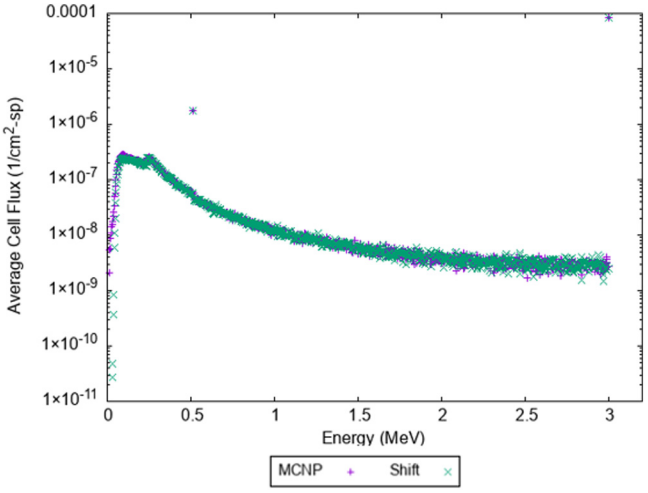

Fig. 12. Average cell flux comparison over the 3 MeV source spectrum. A global maximum value is observed at the 3 MeV energy bin, which corresponds to a photopeak when converted to a pulse height. A local maximum value is observed around the 500 keV energy bin, which corresponds to a 511 keV annihilation peak when converted to a pulse height.

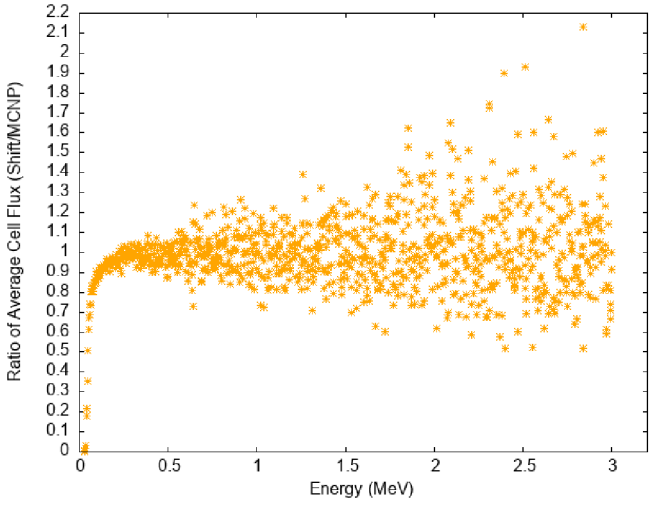

Fig. 13. Ratio of Shift and MCNP average cell flux over the 3 MeV source spectrum.

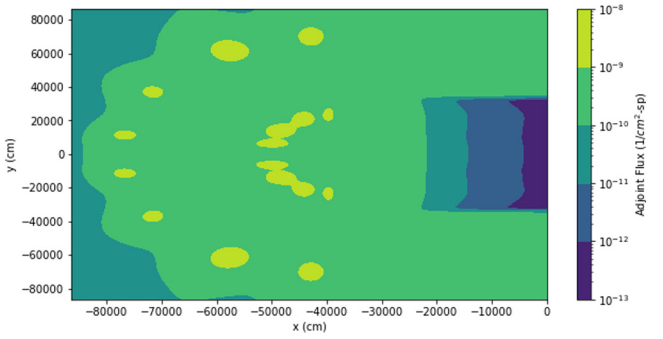

Fig. 14. Group 7 (2.5–3.0 MeV) adjoint flux distribution for a 2″ × 2″ NaI(Tl) detector simulation defined for a 2.54 cm source–detector distance at $x = -2.54$ (soil contamination).

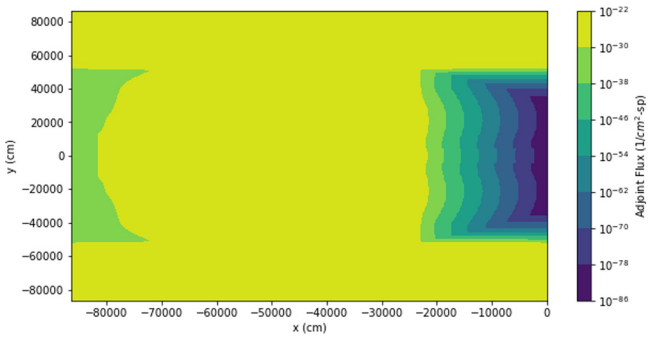

Fig. 15. Group 19 (0.01–0.045 MeV) adjoint flux distribution for a 2″ × 2″ NaI(Tl) detector simulation defined for a 2.54 cm source–detector distance at $x = -2.54$ (soil contamination).

volumes are minuscule relative to the entire CSG model dimensions shown in Figs. 14 and 15.

In Fig. 14, the group 7 adjoint flux distribution highlights the contribution of skyshine to the detector response. At 3 MeV, the photon mean free path in air is approximated at 21,597 cm [25]. At ~2 mean free paths, the adjoint flux distribution begins to approach the upper magnitude (shown in yellow). This indicates that photons may significantly contribute to the detector response after scattering in the air and back towards the model surface due to attenuation in air. Unimportant particle histories will be preferentially killed, and important particle histories will tend to split such that an increasing number of particle histories will interact with the detector (thus, reducing the tally variance). In Fig. 15, the group 19 adjoint flux distribution magnitudes vary much more significantly when moving away from the source and detector regions due to photoelectric effect absorptions dominating in the 0.01 to 0.045 MeV energy range (and thus less scattering occurs). Very little sampling outside of the source and detector regions will take place in the group 19 Shift MC calculation as a result; therefore, lower energy Shift MC solutions tend to converge faster than higher energy counterparts.

4.4. Monoenergetic surface contamination

Surface contamination detector responses (as a function of energy) are displayed for sample monoenergetic simulations. In Figs. 16 and 17, the efficiency curve (i.e., detector response curve) is shown to largely decrease with increasing source–detector distance, as expected. The number of isotropic photons emitted from the soil that deposit energy in the detector crystal decrease with increasing source–detector distance due to the inverse square law, where irradiance decreases in proportion to the square of the distance. In general, the efficiency will increase

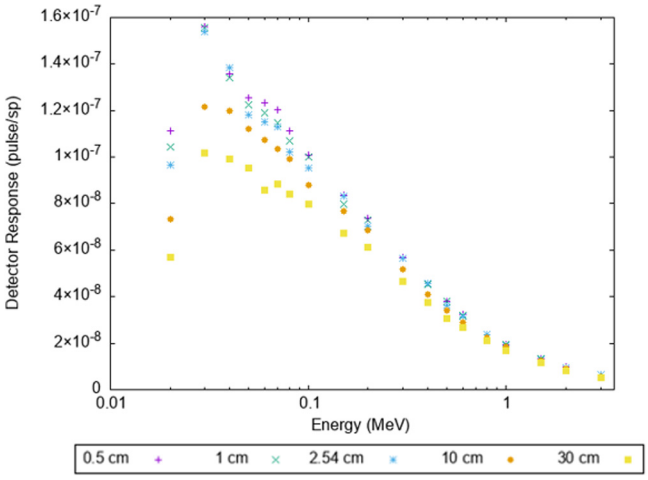

Fig. 16. Soil surface contamination detector response as a function of energy for the 2″ × 2″ detector configuration at each source–detector distance.

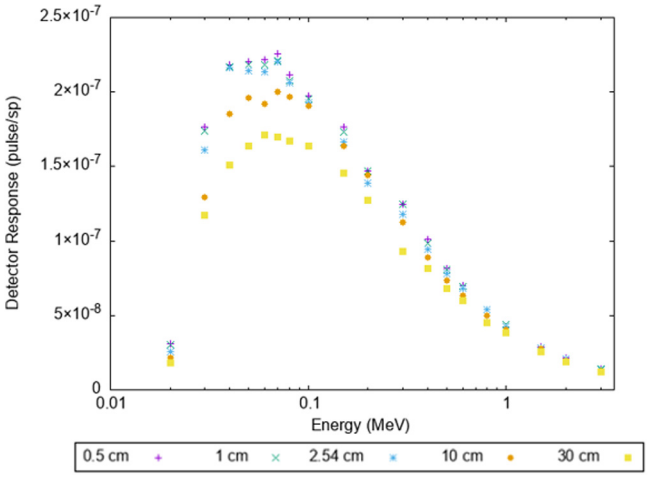

Fig. 17. Soil surface contamination detector response as a function of energy for the 3″ × 3″ detector configuration at each source–detector distance.

to a lower limit at lower energies due to increasing energy deposition through photoelectric effect absorptions in the detector crystal.

The efficiency curve trends in Figs. 18 and 19 may be largely explained by the variations in linear attenuation and any associated buildup between the contaminated media, as shown by Fig. 20 [25]. The fraction of photons that are attenuated as a function of energy for soil and concrete are relatively close in magnitude, whereas a larger difference exists between steel and the remaining media of soil and concrete. The effective atomic number of concrete and soil composition are close to one another compared to their distance to that of steel. More photons will be attenuated due to photoelectric effect, Compton scattering, and/or pair production interactions at each energy in the steel medium. Therefore, fewer photons will be available to interact with the detector crystal at each energy with contaminated steel.

4.5. Monoenergetic volumetric contamination

Volumetric contamination detector responses (as a function of energy) are displayed for sample monoenergetic simulations. It should be noted that results are omitted at select energies in Figs. 21–24 if the prescribed contamination depth exceeds four mean free paths at a given photon energy. As an example, all detector responses for steel in Fig. 23

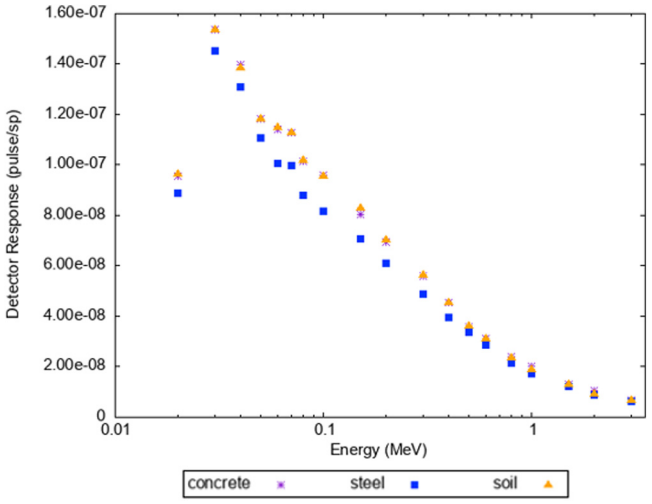

Fig. 18. Surface contamination detector response as a function of energy for the 2″ × 2″ detector configuration for all contaminated media (2.54 cm source–detector distance).

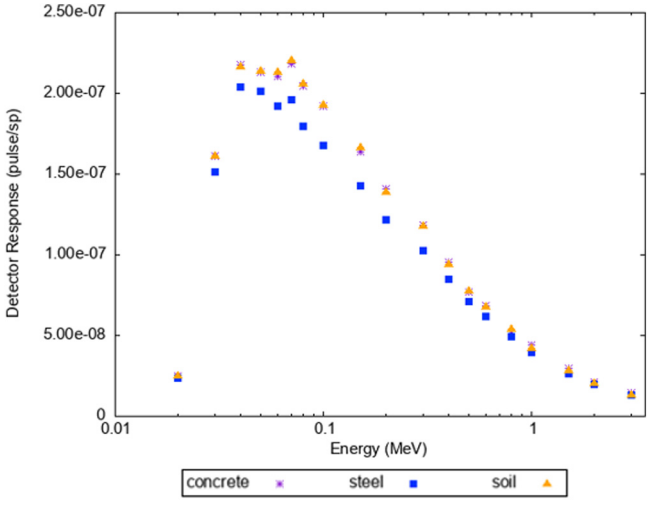

Fig. 19. Surface contamination detector response as a function of energy for the 3″ × 3″ detector configuration for all contaminated media (2.54 cm source–detector distance).

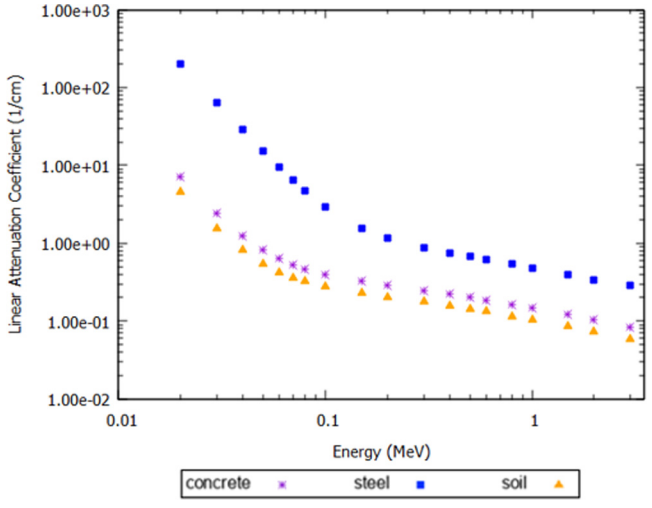

Fig. 20. Linear attenuation coefficient for concrete, steel, and soil as a function of energy.

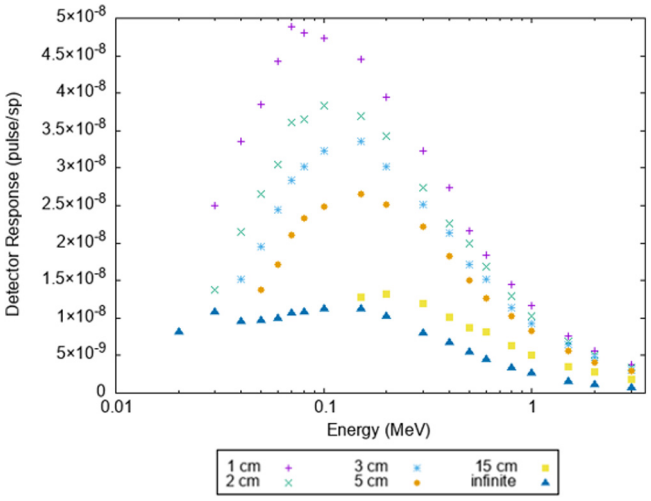

Fig. 21. Soil volumetric contamination detector response as a function of energy for the 2″ × 2″ detector configuration for all contamination depths (source–detector distance of 2.54 cm).

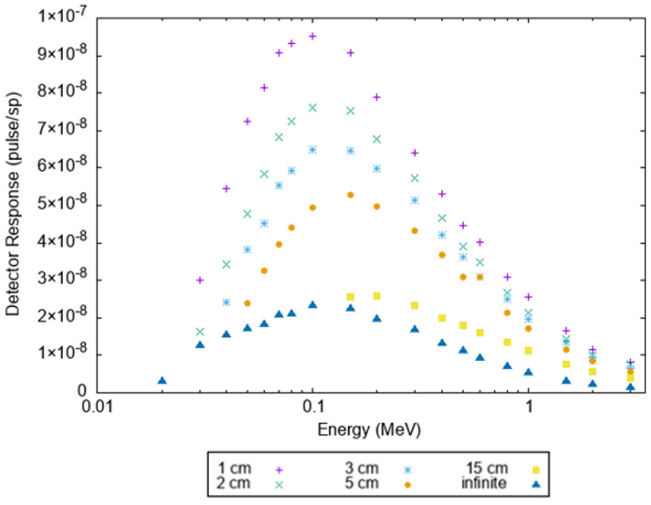

Fig. 22. Soil volumetric contamination detector response as a function of energy for the 3″ × 3″ detector configuration for all contamination depths (source–detector distance of 2.54 cm).

are omitted from 0.02 to 0.15 MeV, since the prescribed contamination depth (3 cm) exceeds four mean free paths in this energy range.

The efficiency curves will decrease as the contamination depth increases at any detector configuration, as shown by Figs. 21 and 22. The infinite depths are not constant; the infinite depths are defined as four mean free paths in the contaminated medium of interest as a function of the source energy. Thus, shifted efficiency curve trends may be observed when compared to those of other contamination depths, which result in seemingly altered efficiency curve trends when compared to all other contamination depths. As expected, the detector response will increase with decreasing contamination depth, since a larger source distribution (flux) will be less attenuated and thus readily interact with the detector crystal.

The efficiency response curves in Figs. 23 and 24 demonstrate larger differences in detector response efficiencies between each contaminated media when compared to Figs. 18 and 19. The buried sources become more heavily attenuated in the media following emission when compared to the surface sources and will therefore vary more significantly with respect to direction throughout the problem environment. Hence, the effect of buildup is pronounced for buried

Table 5
Sample MCNP/Shift volumetric contamination full model comparisons.

Case	Medium	Energy (MeV)	Depth (cm)	Detector	Distance (cm)	MCNP response (pulse/sp)	Shift response (pulse/sp)	Percent error (1σ)
1	Soil	1.0	15	3″ × 3″	30	1.08×10^{-8} ±4.3%	1.06×10^{-8} ±1.2%	1.85%
2	Concrete	0.5	3	2″ × 2″	2.54	1.64×10^{-8} ±3.5%	1.54×10^{-8} ±1.6%	6.10%
3	Steel	0.8	5	3″ × 3″	0.5	7.07×10^{-9} ±4.86%	7.04×10^{-9} ±1.7%	0.42%

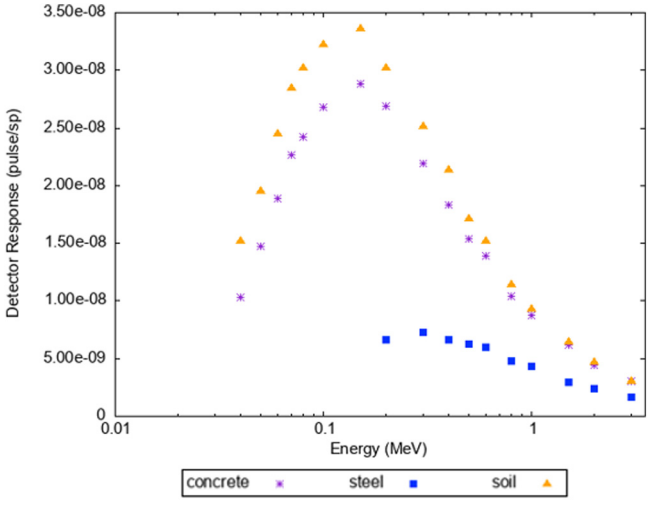

Fig. 23. Volumetric contamination detector response as a function of energy for the 2″ × 2″ configuration for all contaminated media (contamination depth of 3 cm/source–detector distance of 2.54 cm).

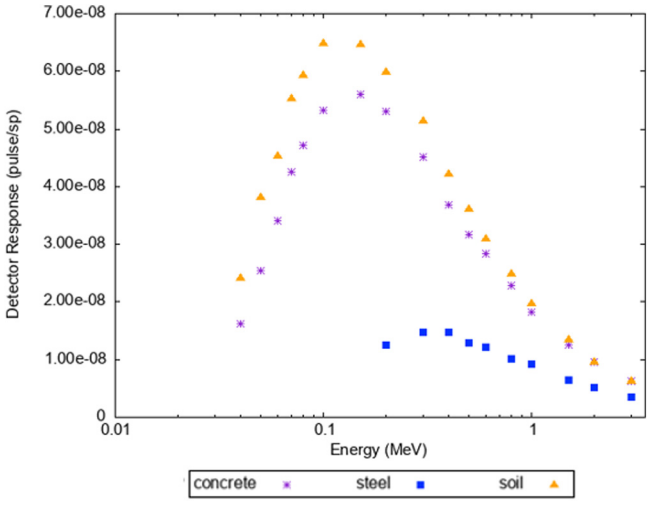

Fig. 24. Volumetric contamination detector response as a function of energy for the 3″ × 3″ configuration for all contaminated media (contamination depth of 3 cm/source–detector distance of 2.54 cm).

source contamination scenarios. Buried source particles may undergo excessive amounts of interactions within the media prior to reaching the surface. Consequently, MC simulations of buried source attenuation problems without the use of optimal weight windows or consistently biased sources are computationally expensive.

Sample comparisons between MCNP full model pulse height simulations and Shift detector response interpolations are shown in Table 5. Currently, the Shift interpolated detector response values are given without associated relative errors; the convergence criterion for volumetric contamination simulations is based upon the Shift average cell flux relative errors (less than 5%). The MCNP and Shift comparison results demonstrate relatively well convergence with equivalent magnitudes.

Table 6
Corresponding Table 5 computer time and FOM comparisons. All MCNP simulations were run on the ORNL Romulus (2.8 GHz AMD Opteron 6320) and Remus (2.4 GHz Intel Xeon CPU E5620) machines. All Shift simulations were run on the ORNL Apollo (2.1 GHz Intel Xeon Silver 4110 CPU) machine; all simulations were run with 8 nodes and 32 CPU cores per node.

Case	Computer Time (CPU-Minutes)		FOM	
	MCNP	Shift	MCNP	Shift
1	6.28×10^{4}	2.03×10^{3}	8.62×10^{-3}	3.28
2	5.85×10^{4}	1.65×10^{3}	1.40×10^{-2}	2.17
3	5.45×10^{4}	1.37×10^{3}	7.78×10^{-3}	2.62

A summary of the computer time and figure of merit (FOM) comparisons between MCNP and the Shift MC solver are shown in Table 6 for the corresponding Table 5 cases. The figure of merit (FOM) may be used as a metric to evaluate the efficiency of the MC simulation and is calculated as follows [14]:

$$FOM = \frac{1}{(R^2 T)}, \tag{6}$$

where R is the tally relative error (fractional standard deviation) and T is the total computer time of all histories in minutes. The FOM values shown for the Shift MC solver were calculated by Eq. (6) using only the Shift MC transport solving times and average cell flux relative errors. The FOM values shown for MCNP were extracted from the generated output files, where the total computer time of all histories and pulse height relative errors were used in the calculations. Since the weight window precalculation method was employed, the majority of the computer time during the entire CADIS hybrid method simulation was dominated by the Shift MC transport runtime. Therefore, the deterministic solver time in Denovo was neglected in the Shift FOM calculation. The VR parameters significantly decreased the total computer time for the Shift MC transport of particles when compared to native MCNP. The efficiency of the MC simulation was greatly improved as a result of the CADIS hybrid VR method, where the FOM was shown to increase by a maximum factor of 381 in Table 6 for Case 1.

5. Conclusions

Modeling research has been conducted in order to demonstrate the feasibility and robustness of combining the capabilities of MCNP with Shift for the acceleration of detector response estimations for thousands of wide-area, complex photon source contamination scenarios. Novel detector response functions coupling MCNP and Shift were developed in order to significantly increase the efficiency of these simulations. The results align with full model MCNP pulse height simulations, dramatically increase MC simulation efficiencies, and exhibit reliable trends. MCNP coupled with Shift for detector response modeling may be applicable to future applications for radiological contamination cleanup, such as cleanup following decommissioning or a radiological dispersion device (RDD) incident, where the use of the MCNP alone for facilitating such large assessments may be computationally limited.

CRediT authorship contribution statement

E. Asano: Methodology, Software, Validation, Formal analysis, Writing – original draft. **D. Coleman:** Software. **G. Davidson:** Methodology, Resources, Writing – review & editing. **S. Dewji:** Conceptualization, Methodology, Software, Supervision, Writing – review & editing.

Declaration of competing interest

The authors declare that they have no known competing financial interests or personal relationships that could have appeared to influence the work reported in this paper.

Acknowledgments

The authors would like to thank Dr. Douglas Peplow and Dr. Cihangir Celik of Oak Ridge National Laboratory, as well as Alex Perry of Texas A&M University for their provided technical expertise throughout the project effort.

References

[1] US Environmental Protection Agency, Multi-agency radiation survey and site investigation manual (MARSSIM), 2022, Available at https://www.epa.gov/radiation/multi-agency-radiation-survey-and-site-investigation-manual-marssim. (Accessed 5 January 2022).

[2] US Environmental Protection Agency, Radiation at superfund sites, 2022, Available at https://www.epa.gov/superfund/radiation-superfund-sites. (Accessed 9 February 2022).

[3] Interstate Technology & Regulatory Council, Determining cleanup goals at radioactively contaminated sites: Case studies, 2022, Available at https://connect.itrcweb.org/HigherLogic/System/DownloadDocumentFile.ashx?DocumentFileKey=6b33e9b6-6db4-41db-852b-70eb0f9ef305. (Accessed 9 February 2022).

[4] United States Nuclear Regulatory Commission, Subpart E to title 10 of the code of federal regulations part 20—Standards for protection against radiation, 2022, Available at https://www.nrc.gov/reading-rm/doc-collections/cfr/part020/full-text.html. (Accessed 9 February 2022).

[5] United States Nuclear Regulatory Commission, Minimum detectable concentrations with typical radiation survey for instruments for various contaminants and field conditions, 2022, Available at https://www.nrc.gov/docs/ML2023/ML20233A507.pdf. (Accessed 9 February 2022).

[6] Christopher J. Werner, et al., MCNP user's manual - code version 6.2, 2022, Available at https://mcnp.lanl.gov/pdf_files/la-ur-17-29981.pdf. (Accessed 5 January 2022).

[7] Seth R. Johnson, et al., Omnibus user manual, 2022, Available at https://info.ornl.gov/sites/publications/Files/Pub120294.pdf. (Accessed 5 January 2022).

[8] Tara M. Pandya, et al., Implementation, capabilities, and benchmarking of shift, A massively parallel Monte Carlo radiation transport code, J. Comput. Phys. 308 (2016) 239–272.

[9] J.C. Wagner, A. Haghighat, Automated variance reduction of Monte Carlo shielding calculations using the discrete ordinates adjoint function, Nucl. Sci. Eng. 128 (1998) 186.

[10] D.E. Peplow, Monte Carlo shielding analysis capabilities with MAVRIC, Nucl. Technol. 174 (2) (2011) 289–313, http://dx.doi.org/10.13182/NT174-289, (Accessed 24 February 2022).

[11] S.W. Mosher, et al., ADVANTG – an automated variance reduction parameter generator, 2022, Available at https://info.ornl.gov/sites/publications/files/pub46035.pdf. (Accessed 5 January 2022).

[12] J.K. Shultis, R.E. Faw, An MCNP primer, 2022, Available at https://www.mne.k-state.edu/~jks/MCNPprmr.pdf. (Accessed 9 February 2022).

[13] C. Kiedrowski Brian, MCNP6 for criticality accident alarm systems – A primer, 2022, Available at https://mcnp.lanl.gov/pdf_files/la-ur-12-25545.pdf. (Accessed 9 February 2022).

[14] X.-M.C. Team, MCNP – A general N-particle transport code, version 5. Volume I: Overview and theory, 2022, Available at https://mcnp.lanl.gov/pdf_files/la-ur-03-1987.pdf. (Accessed 5 January 2022).

[15] T.E. Booth, J.S. Hendricks, Importance estimation in forward Monte Carlo calculations, Nucl. Technol. Fusion 5 (1984) 90–100.

[16] Thomas E. Booth, Genesis of the weight window and the weight window generator in MCNP – A personal history, 2022, available at https://mcnp.lanl.gov/pdf_files/la-ur-06-5807.pdf. (Accessed 9 February 2022).

[17] F.N. Fritsch, J. Butland, A method for constructing local monotone piecewise cubic interpolants, SIAM J. Sci. Comput. 5 (2) (1984) 300–304.

[18] Cleve B. Moler, Numerical Computing with MATLAB, The MathWorks, Inc. Natick, Massachusets, 2004.

[19] Scipy documentation, scipy.interpolate. PchipInterpolator — SciPy v1.7.1 Manual, 2022, Available at https://docs.scipy.org/doc/scipy/reference/generated/scipy.interpolate.PchipInterpolator.html. (Accessed 5 January 2022).

[20] L.L. Carter, R.A. Schwarz, MCNP visual editor computer code manual, 2022, Available at https://www.osti.gov/biblio/88641-mcnp-visual-editor-computer-code-manual. (Accessed 5 January 2022).

[21] Thomas M. Evans, Alissa S. Stafford, Rachel N. Slaybaugh, Kevin T. Clarno, Denovo: A new three-dimensional parallel discrete ordinates code in SCALE, 2022, Available at https://www.tandfonline.com/doi/abs/10.13182/NT171-171. (Accessed 5 January 2022).

[22] John C. Wagner, Douglas E. Peplow, Scott W. Mosher, FW-CADIS method for global and regional variance reduction of Monte Carlo radiation transport calculations, Nucl. Sci. Eng. 176 (2014) 37–57, 1.

[23] Keith F. Eckerman, Jeffrey C. Ryman, Federal guidance report No. 12: External exposure to radionuclides in air, water, and soil (FGR 12), 2022, Available at https://www.ornl.gov/sites/default/files/fgr12.pdf. (Accessed 9 February 2022).

[24] M.B. Bellamy, S.A. Dewji, M. Hiller, K. Veinot, R.P. Manger, K.F. Eckerman, J.C. Ryman, C.E. Easterly, N.E. Hertel, D.J. Stewart, EPA federal guidance report no. 15: External exposure to radionuclides in air, water and soil (FGR 15), 2022, Available at https://www.epa.gov/sites/default/files/2019-08/documents/fgr_15_final_508_2019aug02.pdf. (Accessed 5 January 2022).

[25] J. Hubbell, S. Seltzer, X-ray mass attenuation coefficients, 1996, Available at https://www.nist.gov/pml/x-ray-mass-attenuation-coefficients. (Accessed 5 January 2022).

[26] Autodesk, INC., AutoCAD®, 2022, Available at https://www.autodesk.com/. (Accessed 5 January 2022).

[27] R.J. Mcconn, C.J. Gesh, R.T. Pagh, R.A. Rucker, R. Williams, Compendium of material composition data for radiation transport modeling, 2022, Available at https://www.pnnl.gov/publications/compendium-material-composition-data-radiation-transport-modeling-1. (Accessed 5 January 2022).

[28] B.T. Rearden, M.A. Jessee (Eds.), SCALE code system, 2022, Available at https://info.ornl.gov/sites/publications/files/Pub68918.pdf. (Accessed 5 January 2022).